Experimental analysis of bubble-driven magma motion in the conduit, for persistently-active, open vent volcanoes

Stephen Pansino, Eliza S Calder, Thierry Menand

Experimental analysis of bubble-driven magma motion in the conduit, for persistently-active, open vent volcanoes

Stephen Pansino[1], Eliza S. Calder[2], Thierry Menand[3]

[1] Earth Observatory of Singapore, Nanyang Technological University, 50 Nanyang Ave., 639798, Singapore

[2] School of Geosciences, University of Edinburgh, Grant Institute. The King's Buildings, West Mains Road. Edinburgh EH9 3JW, Scotland, UK

[3] Université Clermont Auvergne, CNRS, IRD, OPGC, Laboratoire Magmas et Volcans, F-63000 Clermont-Ferrand, France

Corresponding author: Stephen Pansino (phone: (+65) 9015-4320; Email: stepheng001@e.ntu.edu.sg or steve.pansino@gmail.com)

Abstract

This study uses analogue experiments to understand the role of bubbles in inducing conduit convection, for persistently degassing lava lake systems. To do so, air was fluxed through an initially stagnant column of liquid and the resulting return flow was measured. The dynamics suggested by the experimental results is compared to that of quiescent, persistently active volcanoes, with a focus on eight volcanoes that exhibit summit lava lakes. We find that magma flux is a function of combined gas flux, conduit size and magma rheology. Experiments with high gas fluxes through low viscosity liquid took on turbulent characteristics, which correspond to high degree of return flow, whereas lower gas fluxes through high viscosity liquids yielded slug flow, which corresponded to less return flow. We model the magma flux due to bubble ascent and find that gas-driven liquid flow can yield faster flow rates than other mechanisms at work in volcanic conduits. This can explain the discrepancy between previous estimates of magma flow in conduits and relatively fast, lava lake surface velocity observations. We show how bubble-driven convective flow can work alongside density-driven convection and discuss the depths in the conduit where each are likely to dominate the system.

Keywords: magma convection, bubble-driven flow, persistent activity, bubble dynamics, two-phase flow

1. Introduction

Volcanoes that host lava lakes or open vents can degas significant quantities of volatiles (10's-100's kg/s) with negligible erupted net flux of lava (Harris *et al.,* 1999; Sawyer *et al.,* 2008a; Sawyer *et al.,* 2008b). Such systems are often characterized by relatively low viscosity basaltic to basaltic-andesitic magmas, which can effectively circulate from depth to surface, while allowing heat and volatiles to permeate through, and out of, the system (Stevenson and Blake, 1998; Witter *et al.,* 2004; Palma *et al.,* 2011). Many such systems, are noteworthy for their longevity, having persisted for decades to millennia (Oppenheimer *et al.,* 2004; Harris *et al.,* 2005; Sweeney *et al.,* 2008; Allard, 2010) and span geologic settings from continental arcs to rift zones.

The stable, long-lived nature of this type of system has been investigated from two schools of thought, both of which rely on a separate model of the magma dynamics in the lava lake and conduit. The first explains that heat is supplied to the surface by density-driven convection in the conduit, in that bidirectional flow efficiently carries heat and volatiles from depth to the surface (Stevenson and Blake, 1998; Huppert and Hallworth, 2007; Palma *et al.,* 2011; Burgi *et al.,* 2014). The rate of convection depends on density and viscosity differences between the ascending, volatile-rich magma and descending, degassed magma (Kazahaya *et al.,* 1994; Becket *et al.,* 2014). In this sense, the gas and magma are well-coupled and the magnitude of heat supply and degassing is a function of how quickly the magma flows. The second school of thought models the magma dynamics as driven by large gas bubbles. In this case, the magma is considered relatively stagnant (in that the circulation of magma is weak) and large gas bubbles carry heat to the surface by bringing warm magma up in their wakes (Jaupart and Vergniolle, 1998; Menand and Phillips, 2007a, b; Pioli *et al.,* 2012; Vergniolle and Bouche, 2016). These large bubbles may leave behind a bubbly wake, which ascend and degas over a period of time (Bouche *et al.,* 2010). In such a scenario, the gas and magma are uncoupled, so the magnitude of heat supply depends on the magnitude and frequency of gas flux. Broadly speaking, both schools of thought agree that the volatiles ascend through the conduit and keep the surface hot, but disagree whether the gas and magma are coupled and therefore whether the magma is circulating.

In order to describe how heat is supplied to the surface, it is important to understand how magma moves through the conduit. The large bubble model has been developed to well-describe how such bubbles behave but, to the best of our knowledge, does not yet incorporate estimates for global magma flow (*i.e.* along the conduit), which may supply heat to the surface. On the other hand, the conduit convection model describes how magma can flow

in the conduit, but has the limitation that magma flow is considered to operate uniformly over the entire length. In the deepest segment of a volcanic conduit, where gas remains dissolved in the melt, the most plausible driving force of magma motion is buoyancy due to fluid density differences. Certainly, when considering small bubbles coupled to the magma, the effects of bubbles are likely constrained to producing bulk density and viscosity variations (Llewellin and Manga, 2005). However, conduit-fed lava lakes, representing the flared top of the conduit, have occasionally been observed to be vigorously active and with fluid motions in a churn-turbulent regime as the gas bubbles and slugs rapidly and constantly buoy up, and rupture on the lake surface (Calder *et al.,* 2004). Such vigorous magma flow, due to bubbles that are large enough to ascend with great velocity, clearly induce motions of the fluid around that, but this is dynamic, and potential for it to contribute to conduit-scale convection has not yet been quantified.

In this work analogue modeling was used to determine the effect of dynamic bubble ascent (henceforth referred to as bubble dynamics) on magma motion in a conduit. In the experiments, gas was fluxed through an initially stagnant liquid in a vertical cylinder. The bubbles induced liquid motion was then studied. Gas flux and liquid viscosity was systematically varied and the liquid velocity was measured. Our study also considers eight, well-studied, persistently active volcanoes for comparison and scaling purposes. These are Villarrica (Chile), Nyiragongo (Democratic Republic of the Congo), Erta ‘Ale (Ethiopia), Kilauea (Pu’u O’o vent, Hawai’i), Mt. Erebus (Antarctica), Masaya (Nicaragua), Stromboli (Italy), and Ambrym (Vanuatu). These are considered to represent a reasonable suite of analogue volcanoes for which bubble-driven conduit motions might play a greater or lesser role in their conduit dynamics. The analogue experiments and their results are described in sections 2 and 3. We then discuss the results in section 4, and place them in the context of natural systems.

2. Methodology

2.1 Experimental apparatus

An analogue model was constructed to represent a magma-filled conduit with gas bubbles passing through it (Fig. 1). To do so, we filled the apparatus with liquid and injected air at the base, using a 1 bar pressure regulator and a set of flow meters to control the flux. We chose a cylindrical shaped apparatus (116.5 cm long x 7 cm diameter) to reflect the shape of the shallowest segment of volcanic conduits, as sometimes visible when lakes drain (Carbone *et al.,* 2013). Small variations in conduit shape and size that are common in natural systems can be then taken into account using the concept of equivalent radius, as proposed by Palma *et al.*

(2011) and also commonly used in engineering practices (White, 2003). The equivalent radius is essentially a length scale that is representative of the overall non-uniform geometry (*e.g.*, the mean radius of the conduit).

The cylinder was filled to a height of 90-104 cm, yielding a length to diameter ratio of 12:1 to 15:1. For a narrow, ~3 m diameter conduit (*e.g.* Stromboli) (Burton *et al.,* 2007), this geometrically scales to a 40 to 50 m section of the conduit. For a larger, ~11 m diameter conduit (*e.g.* Villarrica) (Palma *et al.,* 2011), this corresponds to 130 to 170 m of the conduit. These dimensions may be far from the length scale of an entire conduit, which could be up to kilometers in length, but this simplified apparatus is sufficient to model a shallow segment of the conduit and, importantly, to quantify the effect of rising gas bubbles on liquid movement. Specifically, it best applies to the shallow region where bubbles are large and ascend rapidly and frequently and therefore where bubble dynamics can be reasonably inferred to be significant, but below a depth at which explosive expansion occurs.

2.2 Scaling

2.2.1 Dimensional analysis

A key parameter of bubble-driven fluid convection in a conduit is the density difference $\Delta\rho$ between the two phases (liquid-gas), which can be simplified by neglecting the density of the gas relative to that of the fluid ρ_l, i.e. $\Delta\rho \approx \rho_l$ (see Table 1 for symbols). Furthermore, we anticipate that the liquid velocity v_l that characterizes this bubble-driven convection depends also on the gravitational acceleration g, the dynamic viscosity μ_l of the liquid, the conduit diameter D_c, the size D_b of the bubbles that drive convection and their volumetric flux Q_g. Using dimensional analysis (Barenblatt, 1996), we thus find four dimensionless groups,

$$\Pi_1 = \frac{\rho_l v_l D_c}{\mu_l}, \quad \Pi_2 = \frac{D_b}{D_c}, \quad \Pi_3 = \frac{\rho_l Q_g}{\mu_l D_c}, \quad \Pi_4 = \frac{\rho_l}{\mu_l}\sqrt{g D_c^3}, \tag{1}$$

such that $\Pi_1 = f(\Pi_2, \Pi_3, \Pi_4)$ with f a function that remains to be determined. It follows that the liquid velocity v_l can be expressed as

$$v_l = \frac{\mu_l}{\rho D_c} f\left(\frac{D_b}{D_c}, \frac{\rho Q_g}{\mu_l D_c}, \frac{\rho}{\mu_l}\sqrt{g D_c^3}\right). \tag{2}$$

Although, the function f is as yet undefined, the four dimensionless groups have each some physical meaning that can be used to scale our analogue model to dynamic magmatic conditions:

- $\Pi_1 = \rho_l v_l D_c/\mu_l$ is the Reynolds number for the liquid, Re_l, the ratio of inertial to viscous forces that affect liquid motion in the conduit (e.g. Holman, 2002);

- $\Pi_2 = D_b/D_c$ is the ratio between the size of the conduit and that of the bubbles, and thus it must be related to the gas fraction ε in the conduit;
- $\Pi_3 = \rho_l Q_g/(\mu_l D_c)$ would be the gas Reynolds number, $Re_g = \rho_l v_b D_c/\mu_l$, if the gas phase were to occupy the entire section of the conduit: in this case $Q_g \approx v_b D_c^2$ with v_b the bubble or gas ascent velocity, and $\Pi_3 \approx Re_g = \rho_l v_b D_c/\mu_l$;
- $\Pi_4 = \rho_l (g D_c^3)^{1/2}/\mu_l$ is the dimensionless inverse viscosity, N_f, defined by Wallis (1969, p. 285-288) by equating the characteristic velocity of inertia-dominated flow with that of viscous-dominated flow: $N_f >$ 300 when inertia dominates whereas $N_f < 2$ when viscosity is dominant. Note, however, that this dimensionless number has been defined for the case of a large bubble rising up a conduit of which it occupies almost the entire width, i.e. slug flows (Wallis, 1969).

The Reynolds number is particularly important since it can be related to both dimensionless groups Π_1 and Π_3. Therefore, we give its general form:

$$Re = \frac{\rho_l v L}{\mu_l}, \quad (3)$$

where v and L are characteristic velocity and length scale: later on, the specific liquid Reynolds number, Re_l, and gas Reynolds number, Re_g, will be obtained by using the appropriate parameters for each phase.

2.2.2 Analogue scaling to dynamic magma conditions

In our system, Π_1, Π_2, and Π_3 can be related because the liquid and gas motions are both related to each other and dependent on the gas fraction ε. We consider the gas fraction as the proportion of the horizontal cross-section area of the conduit occupied by the bubbles. The horizontal length scales L_l and L_g of the proportion of the conduit occupied by the liquid and the bubbles, respectively, are therefore related to the gas fraction ε as:

$$L_l = D_c\sqrt{1-\varepsilon}, \text{ and } L_g = D_c\sqrt{\varepsilon}. \quad (4)$$

Thus $\Pi_2 = \sqrt{\varepsilon}$ when L_g corresponds to the actual size of the bubbles. These length scales are related to the liquid and gas superficial velocities, such that $v_b = Q_g/[(\pi/4)L_g^2]$ and $v_l = Q_l/[(\pi/4)L_l^2]$ (Vergniolle and Jaupart, 1986; Pioli *et al.*, 2012). Note that equation 4 assumes a cylindrical geometry for both the liquid and gas phases and is thus most-appropriate for slug flow or annular flow. The L_l can also be envisaged as an equivalent length scale for the liquid phase, whose cross section is a disk of diameter L_l. If we assume the flow in the conduit is

laminar and driven by buoyancy in both the experiments and in nature, so that the gas-liquid density difference, $\Delta\rho$ is similar to ρ_l, then the liquid velocity can be expressed as

$$v_l = \frac{gC\rho_l L_l^2}{\mu_l} = \frac{gC\rho_l D_c^2(1-\varepsilon)}{\mu_l}, \quad (5)$$

where C is a constant of proportionality and equals 1/12 (Batchelor, 1967, p.234-236). This is a first-order approximation of the velocity, which assumes the liquid velocity is driven by the gas buoyancy and resembles the Stoke's bubble rise velocity, which models velocity for any size of bubble (Vergniolle and Jaupart, 1986). As such, we used this velocity scale to estimate the liquid rheologies to be used in our experiments, but will use the actual liquid velocity measurements when we analyze the results. By combining equation 5 for v_l with the general form of the Reynolds number (equation 3), we obtain the liquid Reynolds number, Re_l (which corresponds also to Π_l). This Reynolds number must be identical in nature and in our experiments for these to be scaled properly, and so a relationship independent of velocity can be found between the liquid flow in the experimental and volcanic systems, provided both have similar shapes, hence constant of proportionality C:

$$Re_l = \left(\frac{g\rho_l^2 D_c^3(1-\varepsilon)^{3/2}}{\mu_l^2}\right)_{model} = \left(\frac{g\rho_l^2 D_c^3(1-\varepsilon)^{3/2}}{\mu_l^2}\right)_{magma} \quad (6)$$

which can be rewritten as:

$$\left(\frac{\mu_{l,magma}}{\mu_{l,model}}\right)\left(\frac{\rho_{l,model}}{\rho_{l,magma}}\right) = \left(\frac{D_{c,magma}}{D_{c,model}}\right)^{\frac{3}{2}}\left(\frac{1-\varepsilon_{magma}}{1-\varepsilon_{model}}\right)^{\frac{3}{4}}. \quad (7)$$

This states that the scaled liquid rheology is a function of the scaled conduit diameter and liquid fraction. Note that if we assume turbulent flow conditions in the system, inertial forces have a significant effect on fluid velocity. In this case, equation 5 would become $v_l = C(gD_c)^{1/2}$ (Huppert and Hallworth 2007), and repeating the process once again leads to a relationship slightly different from equation 7:

$$\left(\frac{\mu_{l,magma}}{\mu_{l,model}}\right)\left(\frac{\rho_{l,model}}{\rho_{l,magma}}\right) = \left(\frac{D_{c,magma}}{D_{c,model}}\right)^{\frac{3}{2}}\left(\frac{1-\varepsilon_{magma}}{1-\varepsilon_{model}}\right)^{\frac{5}{4}}. \quad (8)$$

Using published data (Table 2), the scaled liquid viscosity ranges from 10^{-3}-10^{2} Pa·s (analogous liquids are low-viscosity oil to honey), for both laminar and turbulent flow conditions.

Gas flux can be scaled in a similar manner, using the Reynolds number of the gas phase. The ascent velocity of individual bubbles, v_b, is determined following Vergniolle and Jaupart (1986) and Pioli *et al.* (2012):

$$v_b = \frac{v_s}{\varepsilon} = \frac{Q_g}{A_c\varepsilon} = \frac{Q_g}{\frac{\pi}{4}D_c^2\varepsilon} \quad (9)$$

where v_s is the superficial bubble velocity, ε is the gas fraction, Q_g is the gas flux rate and A_c is the cross-sectional area of the conduit. This expression states that the average velocity of the bubbles must be related to the total gas flux and to the proportion of the conduit that the bubbles occupy.

Substituting the relationships obtained for the bubble velocity and the gas length scale (equations 9 and 4) into the general form of the Reynolds number (equation 3) leads to the gas Reynolds number, Re_g, and then yields a relationship between the experimental and natural systems:

$$Re_g = \left(\frac{\rho_l Q_g}{D_c \mu_l \sqrt{\varepsilon}}\right)_{model} = \left(\frac{\rho_l Q_g}{D_c \mu_l \sqrt{\varepsilon}}\right)_{magma}, \varepsilon > 0 \quad (10)$$

Gas flux from volcanoes is generally measured in mass flow rate (*e.g.* kg/s or tons/day). Therefore, equation 10 can be transformed into

$$Re_g = \left(\frac{\rho_l Q_g}{D_c \mu_l \sqrt{\varepsilon}}\right)_{model} = \left(\frac{\rho_l \dot{m}_g}{\rho_g D_c \mu_l \sqrt{\varepsilon}}\right)_{magma} \quad (11)$$

where $\dot{m}_g$ is gas mass flux rate and ρ_g is the volcanic gas density. The scaled gas flux in the experiments ranges from 0.1 to 3.3 L/min, but due to equipment restrictions a minimum flow of only 0.4 L/min was achieved here. A comparison of dimensionless numbers used for scaling is presented in Table 3.

2.3 Experimental setup and procedures

The analogue liquids used were glucose syrup, water, and solutions of the two. Small, suspended bubbles tended to collect in the liquid during the initial pour, so the experiment was allowed to degas overnight to mitigate their potential effects. Small bubbles also tended to accumulate during an experiment and were present in post-experiment measurements. The liquid viscosity was measured before and after each experiment using a disk rotational viscometer, over a range of shear rates. As expected, shear-thinning rheology was observed for the glucose solutions and Newtonian rheology for water. Since the glucose solutions have shear-rate-dependent viscosities, the effective viscosity for each experiment was determined (Table 4) by estimating the shear rate due to bubble ascent. The shear rate is simply approximated to be a function of bubble velocity and the liquid thickness between the bubble and cylinder wall.

The gas flux was controlled using a set of flowmeters, which enabled careful control of the flow rates (Fig. 1). At the beginning of each experiment, the gas was turned on and the system was allowed to stabilize before beginning the experiment. Liquid fill heights were used, as measured before and during experiments, to

201 determine the gas fractions in the cylinder. The gas flux rate was recorded, which was preferred for analysis, as
202 well as bubble diameters and velocities. For turbulent experiments, which had a range of bubble diameters
203 and/or variable bubble velocities (due to liquid flow eddies), mean bubble diameters and averaged velocities
204 over the length of the conduit were used for further analysis.
205
206 Each experiment (documented by video, 1280 x 720 pixels, 1 px ≈ 0.8 mm, 30 fps), began as a few drops of
207 food dye were placed at the liquid free surface. Though the dye has a different density from the experimental
208 liquids (dyes have a density of 0.8 to 1.2 g/mL, depending on color), the small quantities that we used suggest
209 that they did not significantly affect the flow properties and therefore were considered a good proxy for liquid
210 movement. As bubbles ascended, the induced liquid return flow was traced by the dye descent and the dye front
211 velocities were measured. For laminar and transitional flow experiments, the dye remained in concentrated lobes
212 during the entire experiment and the time taken to reach the bottom was measured. For turbulent flow
213 experiments, the dye dispersed throughout the water within the first few seconds, with flow front becoming
214 more dilute with time, so initial velocities were used to indicate the flow.
215
216 **3. Experimental results**
217 *3.1 Observations*
218 We have stored all video recordings of our experiments in a data repository at the doi given in the
219 acknowledgements, which we will qualitatively describe here. In high viscosity experiments (> 1 Pa·s), gas
220 bubbles took on a laminar flow pattern, in which bubbles ascended through the center of the cylinder at a
221 relatively slow, steady speed (Fig. 2a). Bubbles tended to be large, occupying more than half the diameter of the
222 cylinder and were evenly spaced apart vertically. As they ascended through the cylinder, liquid return flow
223 dragged lobes of the dye downward along the annulus of the cylinder with negligible horizontal motion.
224 Downward flow progressed in steps, in that passing bubbles invoked a brief downward motion of the dye front,
225 which otherwise remained motionless. Over the course of an experiment, the average dye velocity was quasi-
226 stable and only changed due to end effects.
227
228 In low viscosity experiments (10^{-3} Pa·s), bubble ascent was relatively unimpeded and higher ascent velocities
229 forced the liquid to move turbulently (Fig. 2b). Bubbles ranged widely in size and large bubbles took up the
230 majority of the diameter of the cylinder. Eddies in the liquid phase induced horizontal as well as vertical

movements of the dye front, which caused the dye to disperse throughout the liquid, making it appear more dilute and homogenous. The dilution of the dye created the artificial appearance that its descent velocity decelerated with depth, typically to 25% to 50% of the initial velocity. For this reason, the initial dye descent velocity, at the start of each experiment, was taken to indicate the actual return flow velocity. In comparison with laminar flow experiments, which took minutes to complete, turbulent flow velocities were significantly faster, requiring only seconds to complete.

A subset of experiments with inviscid syrup (~ 0.1 Pa·s) yielded transitional behaviors. Bubbles tended to be large, but with little variation in size, and ascended chaotically at high velocities. The dye descended in concentrated lobes, without dispersing, but was not confined to the annulus of the cylinder. The arrival of the dye to the bottom of the column was difficult to accurately judge due to the dark syrup color and high velocity, and therefore error for these measurements could be up to ±18% (*i.e.* 2 seconds for dye arrival times in the shortest experiment).

3.2 Dimensionless analysis

We can use physical arguments to estimate the function *f* (equation 2 in the scaling section 2.2) and thus to present our experimental results and to analyze them. The return flow velocities for all experiments are shown against the liquid viscosities and gas flux rates (Fig. 3). Velocities tended to be higher for high gas fluxes and low viscosity liquids. As shown previously (equation 10), combining the gas flux rate, cylinder diameter and liquid rheological properties into the general form of the Reynolds number gives that of the gas phase. In the scaling section, we used the liquid Reynolds number to determine appropriate liquids to use. Here, we have access to liquid velocity data and therefore can calculate its magnitude, by first estimating the volumetric flow rate and the approximate cross-sectional area of the flow. Re_l therefore is

$$Re_l = \frac{\rho_l v_l D_c \sqrt{1-\varepsilon}}{\mu_l} = \frac{\rho_l Q_l}{\frac{\pi}{4} D_c \mu_l \sqrt{1-\varepsilon}}, \quad 0 \le \varepsilon < 1 \tag{12}$$

where

$$v_l = \frac{Q_l}{\frac{\pi}{4} D_c^2 (1-\varepsilon)}. \tag{13}$$

We can express each Reynolds number as a function of two of the four dimensionless groups that were identified in the scaling section 2.2:

$$Re_g = \frac{4}{\pi} \frac{\Pi_3}{\Pi_2}, \quad \text{and} \quad Re_l = \Pi_1 \sqrt{1 - \Pi_2^2}. \tag{14}$$

This means that the function *f* depends in fact on two dimensionless numbers instead of three: $\Pi_1 = f(\Pi_2, \Pi_3, \Pi_4)$ can be simplified as $Re_l = f(Re_g, N_f)$ for instance; the problem can be defined entirely by the dimensionless numbers Re_l, Re_g, and N_f, so that anyone of them can be expressed as a function of the other two.

To see how the individual parameters (Re_l, Re_g, N_f) for all experiments are interrelated and thus determine the form of their interrelationship, they are plotted in 3D (Fig. 4a). For visualization, we also provide 2D plots of Re_g and N_f against Re_l (Fig. 4b, c). The separation between the data groups is due to the way in which the experiments were run and correspond to viscosity differences. The data fit with a log-planar surface using a log-sum-of-squares minimization of the Re_l misfit:

$$Re_l = 0.054 Re_g^{0.75} N_f^{0.49}$$

$$\Leftrightarrow\ Re_l = 0.054 \left(\frac{4\rho_l Q_g}{\pi D_c \mu_l \sqrt{\varepsilon}}\right)^{0.75} \left(\frac{\rho_l}{\mu_l}\sqrt{g D_c^3}\right)^{0.49}$$

$$\Leftrightarrow\ Re_l \cong 0.054 \left(\frac{4\rho_l Q_g}{\pi D_c \mu_l \sqrt{\varepsilon}}\right)^{3/4} \left(\frac{\rho_l}{\mu_l}\sqrt{g D_c^3}\right)^{1/2}. \quad (15)$$

This relationship provides a simple way to characterize the ability of ascending bubbles to cause convection within a conduit, based on relatively static parameters like viscosity and conduit diameter as well as measurable parameters like gas flux.

4. Discussion

4.1 Flux estimates for natural systems

We compare our experimental results, via the same set of dimensionless numbers, to the behavior of eight analogue natural systems, introduced in section 1, which are Villarrica, Nyiragongo, Erta 'Ale, the Pu'u O'o vent of Kilauea, Masaya, Mt. Erebus, Stromboli and Ambrym volcano. We assume that the Re_l can be estimated via equation 15, in which the liquid flux is driven by gas flux. N_f is estimated using the Π_4 relation in equation 1, with parameter values listed in Table 2. Re_g is estimated via equation 11, using the gas mass flux (also listed in Table 2) and approximate gas density. We assume the gas density can be described by the ideal gas law:

$$\rho_g = \frac{PM}{RT} \quad (16)$$

where *P* is magmastatic pressure, *M* is the molar mass of the gas phase, *R* is the ideal gas constant, and *T* is magma temperature. The pressure is estimated at 30 m depth, which is assumed to be a representative depth at which bubbles are large enough to ascend vigorously (we will discuss greater depths in the section 4.3). *M* is estimated from the molar ratios of the gas species that are detected at active volcanoes, which we take from

289 Sawyer *et al.* (2011) and Allard *et al.* (2016). At this depth, the gas density ranges from 0.94 to 2.21 kg/m^3. As
290 we will discuss later in section 4.3, the mass flux depends on the depth, as well as on the volatile molar ratios,
291 and at 30 m depth is approximately 90% of the values listed in Table 2. Using such densities and mass flux
292 values, we estimate the volumetric flux to be 28 +/- 1 m^3/s (Villarrica), 126 +/- 32 m^3/s (Nyiragongo), 13 +/- 2
293 m^3/s (Erta 'Ale), 196 +/- 28 m^3/s (Pu'u O'o), 134 +/- 118 m^3/s (Masaya), 8 +/- 4 m^3/s (Mt. Erebus), 25 +/- 2
294 m^3/s (Stromboli), and 1310 +/- 104 m^3/s (Ambrym). Note that estimating the gas fraction of natural systems is
295 not trivial and we used the procedure described by Pioli *et al.* (2012), which is outlined in Appendix A. All
296 values used to make these estimates for gas fraction, as well as the dimensionless numbers, are listed in Table 2.
297 The Re_l, for two-phase, bidirectional flow, is assumed to scale to the experimentally-derived surface described
298 by equation 15 (Fig. 4a, red tiles). Note that in Fig. 4b and c, the estimates for the natural systems sometimes lay
299 off the experiment trends, since some natural systems have both high gas flux and high viscosities, so that they
300 lay to the right of the trend in Fig. 4b and to the left in Fig. 4c.; however, they lay on the experimentally-derived
301 surface in Fig. 4a. By combining equations 12 and 15, they can be rewritten into a form with dimensions:

302 $$Q_l = \frac{1}{20}\left(\frac{\pi\rho g}{4\mu}\right)^{1/4} Q_g^{3/4} D_c \sqrt{\frac{1-\varepsilon}{\varepsilon^{3/4}}}, \quad 0 < \varepsilon < 1 \qquad (17)$$

303 In the above equation, the magma flux can therefore be estimated using measurements of the magma rheology
304 and gas flux and estimates of the conduit diameter and gas fraction.
305
306 Magma flux has also been estimated in previous studies (Q_l values shown in Table 2), so we can compare with
307 our estimates from equation 17. We find that the magma flux is generally one to two orders of magnitude
308 greater than other studies. The associated axial velocities are on the order of 0.1 to 10 m/s, depending on the
309 system (Fig. 5), which resemble lava lake flow velocities that have been observed to range from a sluggish 0.01
310 m/s (Harris et al., 2005) to a very fast 10 m/s (Pering *et al.*, 2019), depending on the magma supply and
311 degassing rates (Oppenheimer *et al.*, 2009; Allard *et al.*, 2016). Previous estimates of magma flux stem from the
312 magma petrology and from the volatile and thermal flux observed at the lava lake surface, and therefore
313 represent the rate of magma supply. We argue that they reflect the magma motion deep within the plumbing
314 system, but do not account for the dynamics that occur in the shallow system (i.e. due to the motion of bubbles).
315 The relatively-high rates of magma convection that we estimate may reflect observations of vigorous magma
316 motion at lava lakes. Villarrica, for example, has exhibited churn turbulent magma behavior in its summit lava
317 lake (Calder *et al.* 2004, Palma et al., 2011), as well as seismic and acoustic signals that indicate turbulent
318 magma convection in its conduit (Ripepe *et al.* 2010).

319

320 We should also note that our estimates of magma flow are made for confined cylindrical conduits, several
321 meters in diameter, through which large volumes of gas are transported; if 100's of m^3/s of gas pass through a
322 narrow aperture, they will naturally have to take on high velocities. However observations at drained lava lakes
323 reveal that conduits can indeed be narrow at depth but may be larger near the usual lava lake surface level
324 (Carbone *et al.* 2013; Burgi *et al.*, 2014). At depths greater than what can be directly observed, the diameter is
325 usually estimated instead. Since there is uncertainty associated to this parameter, it is helpful to discuss magma
326 flux estimates for larger conduits than shown in Table 2. If we assume that the conduits are larger by some
327 factor (and have a cylindrical geometry), the permissible magma flux in the conduit is proportionally larger, due
328 to equation 17. The associated axial velocity however, is lower by the same factor, due to equation 9. It is
329 unlikely a very high axial velocity could be induced in a constricted geometry (meters in diameter) simply due
330 to passive degassing, since the associated shear forces would be quite high.
331

332 *4.2 A model of bubble-driven magma motion*

333 To link the results of our experiments with field observations of vigorous lava lake motion (Calder *et al.* 2004;
334 Ripepe *et al.* 2010; Palma *et al.* 2011; Allard *et al.* 2016), we introduce a model of bubble-driven convection,
335 which dominates in the shallow region of a conduit, where magmastatic pressure is relatively low and bubbles
336 can vigorously ascend and induce magma overturn. In this model, the bulk fluid flux (bubbles and magma) in
337 any cross section of the conduit is equal for ascending and descending flow. The flux can vary axially however,
338 due to increasing bubble size and bubble ascent velocity. In this sense, the flow rate is lower at the base of the
339 conduit and the higher near the surface. An axial velocity gradient does not conserve mass in a single-phase,
340 one-directional flow within a conduit of constant cross-section, but a bidirectional flow can occur when the
341 ascending component re-entrains part of the descending component. The descending magma is recycled and
342 mingles with ascending magma.
343

344 Recall that, in section 1, we introduced two schools of thought, which both agree that volatiles pass via the
345 conduit from source to surface. The first school explains that the volatile ascent is well-coupled to the magma
346 flux, which results in density-driven convection throughout the length of the conduit (Kazahaya *et al.* 1994;
347 Stevenson and Blake 1998; Huppert and Hallworth 2007; Palma *et al.* 2011; Becket *et al.* 2014; Burgi *et al.*
348 2014). The second school of thought considers the magma and gas to be decoupled, in that the magma is

relatively stagnant and large gas bubbles bring volatiles to the surface, as well as heat from depth in their wakes (Jaupart and Vergniolle 1998; Menand and Phillips 2007a, b; Pioli *et al.* 2012; Vergniolle and Bouche 2016).

Our results show that gas bubble ascent always generates a degree of fluid motion, regardless if the gases take on a bubbly flow or slug flow form. This is also true regardless if the liquid flow is laminar or turbulent, as all experiments plot along the same surface described by equation 15. In the context of the two schools of thought, which disagree on the coupling between the magma and volatiles, our experiments indicate that, yes, volatiles cause magma motion, but no, the two phases are not necessarily well-coupled. If we define that a well-coupled two phase flow has similar velocities for both phases, then bubbly flow is the manifestation of a well-coupled flow and slug flow is the manifestation of a poorly-coupled flow. Both types of bubble ascent generate magma flux at a rate proportional to the gas volumetric flux and negatively proportional to the gas fraction. They are never truly decoupled.

Of particular note is the relationship between the magma flux and the bubble flow pattern. It is known that, for any Newtonian liquid, relatively small gas flux corresponds to bubbly flow, higher flux corresponds to slug flow, and very high flux corresponds to core-annular flow (Pioli *et al.*, 2012). For example, experiments performed with water ranged from bubbly to slug flow patterns, depending on the gas flux, and that high gas flux caused both a high liquid flux and a slug flow pattern to develop. However, 'higher' gas flow patterns (e.g. slug flow) develop more-readily in viscous liquids, as gases build up large bubbles in the conduit (e.g. Fig. 2a). Such experiments tend to have both high gas fractions and low magnitudes of liquid flux, because the liquid viscosity is high. Since these are all two-phase flows, the liquid and gas states affect each other, in that the liquid flux responds to the gas ascent by flowing at a proportional flux, while the gas assumes whatever pattern is preferable to the liquid.

We can conclude that magma motion occurs anywhere that bubbles ascend, however this may or may not affect the entire length of the conduit. At depth, volatiles are under great pressure and tend to be dissolved in the magma. Bubbles that do exist, suspended in the magma, are likely to be small, so their associated ascent dynamics are quite weak. By extension, the magma convection due to such bubbles is also likely to be insignificant. However, it is known that gases can accumulate at discontinuities in the plumbing system,

forming larger slug bubbles, which can ascend from great depths (Burton *et al.*, 2007; Lyons *et al.*, 2010; Menand and Phillips, 2007a,b). Such large bubbles are likely to induce convection regardless of depth.

4.3 Bubble driven motion at depth

We attempt to estimate the magma flux throughout the conduit. Since bubble-driven motion is by definition dependent on gas flux, we first need to estimate the volumetric gas flux at depth. This is primarily dependent on pressure, which directly affects the gas volume (low pressure corresponds to a relatively large gas volume), as well as the available gas mass (low pressure corresponds to a relatively large mass of exsolved volatiles). The pressure at any depth, h, in the conduit is estimated via the magmastatic pressure plus atmospheric pressure, P_{atm}, and is linked to the density via the ideal gas law,

$$\rho_l g h + P_{atm} = \frac{\rho_g RT}{M} \quad , \tag{18}$$

which, in turn, corresponds to the volume flux and mass flux,

$$\rho_g = \frac{\dot{m}_g}{Q_g} = \frac{\Sigma\left(\dot{m}_{spec} e^{-h/h\,spec}\right)}{Q_g} \quad . \tag{19}$$

In the preceding equations, M is the combined molar mass of the gases, R is the ideal gas constant and T is temperature, which we assume is 1400 K. We approximate the mass flux to a summation of exponential functions for the main volatile species, H_2O, CO_2 and SO_2. The measured mass flux of each species, $\dot{m}_{spec}$, is thereby scaled down relative to their characteristic exsolution depths, h_{spec} (values from Parfitt and Wilson 2008). Observed molar ratios of gases emitted from the selected volcanoes are taken from Sawyer *et al.* (2011) and Allard *et al.* (2016).

This is admittedly a rough approximation of the total gas mass flux at depth, however it produces exsolution curves roughly similar to those form more-robust models like VolatileCalc (Newman and Lowenstern, 2002). For example, in comparison to the modeling of exsolved gases done by Allard *et al.* (2016), this method generates similar-shaped molar ratio curves (Fig. 6a), though it tends to underestimate the amount of exsolved H_2O and overestimate the exsolved CO_2 to a degree. However, by estimating the gas mass flux (Fig. 6b) and density (Fig. 6c) at depth, it generates a sensible, first-order approximation of the gas volumetric flux (Fig. 6d). We can similarly estimate the gas fraction at depth (Fig. 6e), via the methodology described in Appendix A, which follows Pioli et al. (2012). The magma flux at depth can therefore be estimated using equation 17, the estimates of gas volumetric flux, gas fraction and the values listed in Table 2 (Fig. 6f).

In addition to being an approximation, there are some limitations to this approach that should be addressed. Volcanic gases may not exsolve in such a simple manner (one dependent entirely on pressure), in part due to interaction between different species, the presence of nucleation points such as crystals, and probably a litany of other factors (Parfitt and Wilson 2008). Presumably, such factors would imply the total gas flux is higher at depth than estimated via equations 18 and 19. Additionally, this model also assumes that the ideal gas law applies, which at high pressures does not, since gases at high temperatures and pressures exist as supercritical fluids and thereby have comparatively high densities and small volumes (Gonnermann and Manga 2013). At high pressures, volatiles in the supercritical state likely have a small volumetric flux and the corresponding magma flux would also be small. As they ascend and depressurize, they reach their critical pressures (such pressures are noted in Kwah *et al.* 2017) and transition to the gas state, which corresponds to a change in density and by extension volume. Our model is capable of estimating the gas density to be high under high pressure (Fig. 6c), but this does not necessarily represent realistic values of density. Assuming a simple hydrostatic pressure relationship, the supercritical fluid to gas phase transition occurs at ~1 km depth for H_2O (critical pressure of 22.1 MPa) and several hundred meters depth for CO_2 (critical pressure of 7.4 MPa; Fig. 6g and h). It is feasible that, as volatiles ascend and transition from the supercritical to the gas state, they increase in volume, causing a sudden transition in the magma flow characteristics. Finally, as discussed in the previous section, we can consider gas slugs, which may form at the roof of a magmatic reservoir or at discontinuities along the conduit. Such bubbles, which maintain large volumes as they ascend through the conduit, induce magma flux regardless of depth.

At any rate, the pressure dependence of exsolved volatiles, and therefore gas flux, upon which we rely is well-established (Newman and Lowenstern, 2002; Burton *et al.*, 2007; Allard *et al.*, 2016) and it is useful to estimate the bubble-driven flux at depth. If we apply the parameters shown in Table 2 to equations 17, 18 and 19, we can get a sense of the gas flux and associated magma flux at depth, for various quiescent, open-vent volcanoes (Fig. 6f). In comparison to previous estimates of magma flux (also shown in Table 2), we predict higher magnitudes in the shallowest 100's of meters of the conduit and similar fluxes for the deeper part. For example at Villarrica, we can compare our model of magma flux as a function of depth with estimates made by Palma *et al.* (2011; Fig. 6g). For the shallowest 100 m, we model the flux to be a factor of 10-100 greater, whereas for depths greater than the volatile critical pressures (400-1000 m), the model flux is similar to their estimates. For Mt. Erebus (Fig.

6h), we estimate that the magma flux in the shallow conduit is higher than previous estimates made by Oppenheimer et al. (2009), by a similar factor of 10-100; magma flux is again similar to Oppenheimer et al. (2009) in the deeper conduit. Considering that the magma flux estimates shown in Table 2 represent a constraint on the magma supply and that they match with our estimates in the deeper part of the conduit, we expect that they indicate the magnitude of flow at the base of the conduit. As volatiles ascend past the depth which correspond to their critical pressures, bubble-driven motion likely becomes increasingly dominant.

4.4 Components of convection

As alluded to throughout this discussion, we argue that our model of bubble dynamics can complement previous models and that these mechanisms dominate at different depths and under different conditions. As such we present a conceptual model of quiescent conduit flow (Fig. 7). At great depth, volatile bubbles are small and generally constrained to impart a buoyancy force on the surrounding magma, in the form of a bulk density difference with cooler, degassed magma descending from the surface. As they ascend, they grow in volume and increase in velocity, which can induce turbulent motion (Fig. 7a). At a critical pressure, they change from supercritical fluid to the gas phase, which is accompanied by a drop in density and increase in volume. Further depressurization due to ascent causes them to continue to grow and accelerate, so that they may be able to induce turbulent overturn of the magma (Fig. 7b). The associated magma velocity along the conduit also increases with bubble velocity, such that magma flux is lower at depth and higher in the shallowest segment (Fig. 7c).

We separate the driving processes of convection into two components (Fig. 7d), which are: density-driven convection due to temperature and compositional variations (1); bubble-ascent-driven magma motion due to discrete, deeply-sourced, slug bubbles (2a) or due to other bubbles which significantly grow as they ascend due to depressurization and exsolution (2b). (1) is uniform along the conduit and is governed by the thermal flux from the lava lake surface and the degree of dissolved volatiles in the ascending and descending magma. (2a) is independent of depth, as slug bubbles ascend at a constant velocity that depends on the film thickness between the bubble and conduit wall. Magma movement is temporary and occurs only as a bubble passes. (2b) becomes more significant near the surface, where the bubbles' collective momentum are greatest. We argue that previous estimates of magma flux, due to density-driven convection, may represent a lower constraint on flux in the conduit, whereas our estimates, due to bubble dynamics, may represent an upper constraint. Similarly, density-

driven convection likely better-describes magma flow at the base of the conduit, whereas bubble dynamics is better applicable to the shallower regions.

5. Conclusion

This study uses analogue experiments to investigate the nature of magma motion in a conduit whose motions is driven by gas flux. The experimentally-derived data was obtained using a range of liquid viscosities and gas fluxes. Our results reveal a power law relationship between the Reynolds numbers of the liquid and gas phases and the dimensionless inverse viscosity (equation 15), in that the magma flow rate is higher for higher gas fluxes and lower viscosity magmas. Applying this relationship to selected natural systems, the magnitude of magma circulation is estimated due to this relationship and is generally one to two orders of magnitude greater than estimates in other studies.

Our estimates account for observations of high flow rates at vigorously active lava lakes and may represent an upper constraint on the magma flux of passively-degassing systems. We expect that magma motion is dominantly driven by bubble ascent near the surface and dominantly driven by density differences at depth. We also expect that the driving mechanism transitions from density-driven to bubble-driven at a depth that is defined by the critical pressures of the volatiles. At this depth, volatiles undergo a state change from supercritical fluid to gas, which causes a decrease in density and increase in volume and occurs at a depth range of several hundred meters to one kilometer.

This work provides a bridge linking two previous models of conduit dynamics. Density-driven convection and large bubble dynamics both operate as a function of the gas flux through the conduit and, in both cases, bubbles cause magma motion.

Acknowledgements

We would like to thank Andrew Harris for his guidance and assistance with this study while the lead author was on an exchange visit to Clermont-Ferrand. Additionally, we thank Ben Van Wyk de Vries for providing the consumables used to perform the experiments and the Tate and Lyle company for their generous provision of golden syrup. This research was partially funded by the International Masters in Volcanology and Geotechniques (INVOGE) program, which is supported by the USA Department of Education – Fund for the Improvement of Postsecondary Education, ATLANTIS program. Our raw data is a collection of video files and

497 handwritten notes. Data from handwritten notes are reflected in Table 4 and the video files are available for
498 download at: https://doi.org/10.21979/N9/Q9HFBE. This is under DR-NTU, a local instance of Dataverse,
499 supported by Nanyang Technological University. This is Laboratory of Excellence ClerVolc contribution
500 number 337.
501

References

Allard P (2010) A CO_2-rich trigger of explosive paroxysms at Stromboli basaltic volcano, Italy. J Volcanol Geotherm Res 189:363-374. doi:10.1016/j.jvolgeores.2009.11.018

Allard P, Aiuppa A, Bani P, Métrich N, Bertagnini A, Gauthier P-J, Shinohara H, Sawyer G, Parello F, Bagnato E, Pelletier B, Garaebiti E (2015). Prodigious emission rates and magma degassing budget of major, trace and radioactive volatile species from Ambrym basaltic volcano, Vanuatu island Arc. J Volcanol Geotherm Res 322, 119-143. doi: 10.1016/j.jvolgeores.2015.10.004

Allard P, Burton M, Sawyer G, Bani P (2016) Degassing dynamics of basaltic lava lake at a top-ranking volatile emitter: Ambrym volcano, Vanuatu arc. Earth Planet Sci Lett 448, 69-80.

Barenblatt, GI (1996). Scaling, self-similarity, and intermediate asymptotics. Cambridge University Press.

Batchelor, GK (1967). An introduction to fluid dynamics. Cambridge University Press.

Becket FM, Burton M, Mader HM, Phillips JC, Polacci M, Rust AC, Witham F (2014). Conduit convection driving persistent degassing at basaltic volcanoes. J Volcanol Geotherm Res 283, 19-35.

Bouche E, Vergniolle S, Staudacher T, Nercessian A, Delmont J-C, Frogneux M, Cartault F, Le Pichon A (2010) The role of large bubbles detected from acoustic measurements on the dynamics of Erta 'Ale lava lake (Ethiopia). Earth Planet Sci Lett 295:37-48. doi:10.1016/j.epsl.2010.03.020

Burgi P-Y, Darrah TH, Tedesco D, Eymold WK (2014) Dynamics of the Mount Nyiragongo lava lake. J Geophys Res Solid Earth 119:4106-4122. doi:10.1002/2013JB010895

Burton MR, Mader HM, Polacci M (2007) The role of gas percolation in quiescent degassing of persistently active basaltic volcanoes. Earth Planet Sci Lett 264:46-60. doi:10.1016/j.epsl.2007.08.028

Calder ES, Harris AJL, Peña P, Pilger E, Flynn LP, Fuentealba G, Moreno H (2004) Combined thermal and seismic analysis of the Villarrica volcano lava lake, Chile. Revista Geológica de Chile 31:2:259-272. doi:10.4067/S0716-02082004000200005.

Carbone D, Poland MP, Patrick MR, Orr TR (2013). Continuous gravity measurements reveal a low-density lava lake at Kilauea Volcano, Hawai'i. Earth Planet. Sci. Lett. 376, 178-185. doi: http://dx.doi.org/10.1016/j.epsl.2013.06.024

Gonnermann HM, Manga M (2013). Dynamics of magma ascent in the volcanic conduit. *In* Modeling Volcanic Processes. Cambridge University Press.

Harmathy TZ (1960) Velocity of large drops and bubbles in media of infinite or restricted extent. J AIChE 6:281-288. doi:10.1002/aic.690060222

Harris AJL, Flynn LP, Rothery DA, Oppenheimer C, Sherman SB (1999) Mass flux measurements at active lava lakes: Implications for magma recycling. J Geophys Res104:B4:7117-7136. doi:10.1029/98JB02731

Harris AJL, Carniel R, Jones J (2005) Identification of variable convective regimes at Erta 'Ale Lava Lake. J Volcanol Geotherm Res 142:207-223. doi:10.1016/j.jvolgeores.2004.11.011

Holman JP (2002) Heat Transfer. McGraw-Hill.

Huppert H, Hallworth M (2007) Bi-directional flow in constrained systems. J Fluid Mech 578:95-112. doi:10.1017/S0022112007004661

Jaupart C, Vergniolle S (1998) Laboratory models of Hawaiian and Strombolian eruptions. Nature 331:58-60. doi:10.1038/331058a0

Kazahaya K, Shinohara H, Saito G (1994) Excessive degassing of Izu-Oshima volcano: magma convection in a conduit. Bull Volcanol 56:207-216. doi:10.1007/BF00279605

Kwah KY, Parat MO, Shaw PN, Falconer JR (2017). Solvent supercritical fluid technologies to extract bioactive compounds from natural sources: A review. Molecules 22, 1186, doi:10.3390/molecules22071186

Lautze NC, Houghton BF (2007) Linking variable explosion style and magma textures during 2002 at Stromboli volcano, Italy. Bull Volcanol 69:445-460. doi:10.1007/s00445-006-0086-1

Llewellin E and Manga M (2005) Bubble suspension rheology and implications for conduit flow. J Volcanol Geotherm Res 143:205-217. doi:10.1016/j.jvolgeores.2004.09.018

Lyons JJ, Waite GP, Rose WI, Chigna G (2010). Patterns in open vent, Strombolian behavior at Fuego volcano, Guatemala, 2005-2007. Bull Volcanol 72, 1-15. doi: 1s00445-009-0305-7

Menand T, Phillips JC (2007a) Gas segregation in dykes and sills. J Volcanol Geotherm Res 159:393-408. doi:10.1016/j.jvolgeores.2006.08.003

Menand T, Phillips JC (2007b) A note on gas segregation in dykes and sills at high volumetric gas fractions. J Volcanol Geotherm Res 162:185-188. doi:10.1016/j.jvolgeores.2007.03.002

Mittelstaedt E, Garcia MO (2007) Modeling the sharp compositional interface in the Pu'u O'o magma reservoir, Kilauea volcano, Hawai'i. Geochem Geophys Geosyst 8:5:Q05011. doi:10.1029/2006GC001519

Newman S, Lowenstern JB (2002). VOLATILECALC: a silicate melt-H_2O-CO_2 solution model written in Visual Basic for excel. Comp Geosci 28:597-604. doi: 10.1016/S0098-3004(01)00081-4

Oppenheimer C, McGonigle AJS, Allard P, Wooster MJ, Tsanev V (2004) Sulfur, heat, and magma budget of Erta 'Ale lava lake, Ethiopia. Geology 32:6:509-512. doi:10.1130/G20281.1

Oppenheimer C, Lomakina AS, Kyle PR, Kingsbury NG, Boichu M (2009) Pulsatory magma supply to a phonolite lava lake. Earth Planet Sci Lett 284:392-398. doi:10.1016/j.epsl.2009.04.043

Palma J, Blake S, Calder E (2011) Constraints on the rates of degassing and convection in basaltic open-vent volcanoes. Geochem Geophys Geosyst 12:11. doi:10.1029/2011GC003715

Parfitt L, Wilson L (2008) Fundamentals of physical volcanology. Blackwell Science Ltd.

Pering TD, Ilanko T, Wilkes TC, England RA, Silcock SR, Stanger LR, Willmott JR, Bryant RG, McGonigle AJS (2019). A rapidly convecting lava lake at Masaya Volcano, Nicaragua. Front Earth Sci 6, 241. doi: 10.3389/feart.2018.00241

Pioli L, Bonadonna C, Azzopardi BJ, Phillips JC, Ripepe M (2012) Experimental constraints on the outgassing dynamics of basaltic magmas. J Geophys Res 117:B03204. doi:10.1029/2011JB008392.

Ripepe M, Marchetti E, Bonadonna C, Harris AJL, Pioli L, Ulivieri G (2010) Monochromatic infrasonic tremor driven by persistent degassing and convection at Villarrica Volcano, Chile. Geophys Res Lett 37:L15303. doi:10.1029/2010GL043516

Rymer H, van Wyk de Vries B, Stix J, Williams-Jones G (1998) Pit crater structure and processes governing persistent activity at Masaya Volcano, Nicaragua. Bull Volcanol 59:345-355. doi:10.1007/s004450050196

Sawyer GM, Carn SA, Tsanev VI, Oppenheimer C, Burton M (2008a) Investigation into magma degassing at Nyiragongo volcano, Democratic Republic of the Congo. Geochem Geophys Geosyst 9:2. doi:10.1029/2007GC001829

Sawyer GM, Oppenheimer C, Tsanev VI, Yirgu G (2008b) Magmatic degassing at Erta 'Ale volcano, Ethiopia. J Volcanol Geotherm Res 178:837-846. doi:10.1016/j.jvolgeores.2008.09.017

Sawyer GM, Salerno GG, Le Blond JS, Martin RS, Spampinato LS, Roberts TJ, Marther TA, Witt MLI, Tsanev VI, Oppenheimer C (2011) Gas and aerosol emissions from Villarrica volcano, Chile. J Volcanol Geotherm Res 203:62-75. doi:10.1016/j.jvolgeores.2011.04.003

Seyfried R, Freundt A (2000) Experiments on conduit flow and eruption behavior of basaltic volcanic eruptions. J Geophys Res 105:B10:23727-23740. doi:10.1029/2000JB900096

Stevenson DS, Blake S (1998) Modelling the dynamics and thermodynamics of volcanic degassing. Bull Volcanol 60:307-317. doi:10.1007/s004450050234

Stix J (2007) Stability and instability of quiescently active volcanoes: The case of Masaya, Nicaragua. Geology 35:6:535-538. doi:10.1130/G23198A.1

Sutton AJ, Elias T, Gerlach TM, Stokes JB (2001). Implications for eruptive processes as indicated by sulfur dioxide emissions from Kīlauea Volcano, Hawai'i, 1979-1997. J Volcanol Geotherm Res 108, 283-302. doi: 10.1016/S0377-0273(00)00291-2

Sweeney D, Kyle PR, Oppenheimer C (2008) Sulfur dioxide emissions and degassing behavior of Erebus volcano, Antarctica. J Volcanol Geotherm Res 177:725-733. doi:10.1016/j.jvolgeores.2008.01.024

Vergniolle, S., Jaupart, C. (1986). Separated two-phase flow and basaltic eruptions. *J. Geophys. Res.*, **91**, B12, 12842-12860. doi: 10.1029/JB091iB12p12842

Vergniolle S, Bouche E (2016). Gas-driven lava lake fluctuations at Erta 'Ale volcano (Ethiopia) revealed by MODIS measurements. Bull Volcanol 78:60. doi: 10.1007/s00445-016-1047-y.

Viana F, Pardo R, Yánez R, Trallero JL, Joseph DD (2003) Universal correlation for the rise velocity of long gas bubbles in round pipes. J Fluid Mech 494:379-398. doi:http://dx.doi.org/10.1017/S0022112003006165

Wallis GB (1969) *One-dimensional two-phase flow*. New York, NY: McGraw-Hill.

White F (2003) Fluid mechanics, fifth ed. McGraw Hill.

Witter JB, Kress VC, Delmelle P, Stix J (2004) Volatile degassing, petrology, and magma dynamics of the Villarrica lava lake, Southern Chile. J Volcanol Geotherm Res 134:303-337. doi:10.1016/j.jvolgeores.2004.03.002

Table and figure descriptions

Table 1 A list of symbols and subscripts used in this article.

Table 2 Literature data of parameters reported for the selected volcanoes used in this study. Gas fractions are estimated using the method discussed by Pioli *et al.* (2012) and summarized in Appendix A.

Table 3 Dimensionless numbers for the experiments in this study and for passively degassing volcanoes. Reynolds number (*Re*) is split into gas and liquid components. Also shown is the dimensionless inverse viscosity (N_f).

Table 4 Experimental data and results. The corresponding values of relevant dimensionless number are included.

Fig. 1 A schematic figure of the experimental apparatus. Air of influx Q_g, permeates through an initially stagnant liquid of density, ρ_l, and viscosity μ_l. Food dye acts as a proxy for return flow velocity, as shown in the inset, which is used to estimate the liquid flux, Q_l. The dimensionless numbers on which this study relies, Re_l, Re_g and N_f are functions of the parameters shown in this figure (respectively equations 12, 10 and Π_4 in equation 1).

Fig. 2 Sequential photographs of experiments. White arrows mark the location of the dye front. (a) Slug bubbles ascend at a steady velocity and the dye descends along the cylinder walls and has a discernible front. Here, the flux is ~2 L/min and the liquid viscosity is ~40 Pa·s. This preliminary experiment is shown for its high visual clarity, but due to uncertainties on the experimental parameters is not shown in Table 4, nor is it further analyzed. (b) Bubbly flow induces a chaotic ascend. Dye disperses throughout the liquid and the front becomes faint with time. Here, the flux is 0.8 L/min and the liquid viscosity is 1 mPa·s (Table 4, 5th row of water section).

Fig. 3 Liquid return flow velocities (Table 4), against viscosity and gas flux. Note that experiments with high viscosity liquid were constrained to lower gas flux rates, to mitigate gas build up in the apparatus.

Fig. 4 (a) The liquid Reynolds number, Re_l, of the experiments (values in Table 4) are plotted against the gas Reynolds number, Re_g, and dimensionless inverse viscosity, N_f. Each experiment is represented by a black dot. We show a best-fitting, log-planar surface described by equation 15. We also show estimates for the volcanoes considered in this study (red polygons), using values from Table 2. (b, c) For visibility, we show 2D plots of Re_g and N_f against Re_l. Estimates for the selected volcanoes are shown by the boxes. The abbreviations are: A (Ambrym), EA (Erta ‘Ale), EB (Mt. Erebus), M (Masaya), N (Nyiragongo), P (Pu’u O’o), S (Stromboli), V (Villarrica). Black abbreviations correspond to the nearest box and colored abbreviations correspond to the similarly-colored box.

Fig. 5 Comparison of flux and velocity estimates for selected natural systems, from this and previous studies. Both subfigures have the same horizontal axis, with labels described in Fig. 4. (a) Magma flux, in which the white bars show median values from Table 2, with the range of values represented by the error bars. Our estimates are made via equation 17 (grey bars). (b) Corresponding axial velocities. All velocities are estimated via equation 13, for the fluxes shown in (a).

Fig. 6 Estimates of gas and magma flux at depth. (a) Molar ratios for major volatile species, for an example of Ambrym volcano, approximated via equation 19. (b) For each of the selected volcanoes, we show the total gas mass flux at depth. Symbol abbreviations are as in Fig. 4. (c) Gas density. (d) Gas volume flux, which depends on estimates shown in (b) and (c). (e) Gas fraction. (f) Magma flux, which depends on the estimates shown in (d) and (e), via equation 17. The grey region indicates the range of flux estimates from previous studies, shown in Table 2. (g, h) Similar plots to (f), focusing respectively on the examples of Villarrica and Mt. Erebus volcanoes, for gas emission rate of 48 and 16 kg/s. The grey regions indicates estimates from previous studies.

Fig. 7 Conceptual model of bubble-driven convection in volcanic conduits. (a) Small bubbles take on linear, laminar ascent. As they grow, they become more turbulent and induce wiggling motion. (b) Bubbles change from supercritical fluids to gas at the critical depth level, causing a decrease in density. Further depressurization may allow them to accelerate and become turbulent (at the turbulence level). (c) Magma velocity similarly increase with bubble velocity. (d) Lines represent components of convection: density differences, $\Delta\rho$, due to heat and volatile content; bubble dynamics for both deeply-sourced slugs and shallow bubbly flow. Slopes indicate either a constant (vertical) or an increasing (inclined) effect with ascent.

Fig. 8 Experimentally-derived K values for equation 21. We categorize experiments via the bubble characteristics, in which slug bubbles are longer than they are wide, bubbly flows contain many, similarly-sized bubbles, and transitional flows contain large, but non-slug bubbles.

Appendix A: Estimating gas fraction

To estimate the gas fractions in the conduits of the selected volcanoes, ε, a method is used following Pioli *et al.* (2012), who give an in-depth discussion of the relationship between gas fraction, gas flux, and bubble velocity. The gas fraction in the conduit is related to the superficial velocity of the gas phase (Eq. 4) and the drift velocity of a bubble, v_d, which is its ascent velocity relative to the liquid phase:

$$\varepsilon = \frac{v_s}{C_0 v_s + v_d} \tag{20}$$

560 C_0 is a parameter that conveys the velocity profile in a cylinder, and is a function of the Eötvös number. For low
561 viscosity liquids undergoing turbulent flow, the parameter varies from 1.2 to 1.4, while for laminar flow, it
562 approaches 2.29 (Viana *et al.* 2003; Pioli *et al.* 2012). We estimate it as described by Pioli *et al.* (2012) and, for
563 the selected volcanoes in this study, it tends to approach 2.29.
564
565 For slug flow, the drift velocity is related to the Froude number, whereas for bubbly flow, it is related to the
566 density and surface tension, σ, of the liquid phase:

567 $$v_d = K\left(\frac{\sigma g(\rho_l - \rho_g)}{\rho_l^2}\right)^{\frac{1}{4}} \quad (21)$$

568 The surface tension for water, syrup, and magma, are respectively 0.07, 0.08, and 0.4 N/m (Seyfried and
569 Freundt 2000). *K*, another empirical parameter, has previously been approximated to 1.53 (Harmathy, 1960).
570 Assuming that the drift velocity equals the difference between the bubble's apparent velocity and the liquid
571 velocity, $v_d = v_b - v_l$, the *K* value can be approximated experimentally (Fig. 8). In this study, it can be seen that
572 *K* values tend to exceed 1, or approaches 1.53 following Harmathy (1960), for bubbly flows. This implies that
573 the drift velocity is high; *i.e.* bubbles move fast relative to the flow velocity of the liquid phase. For slug flow,
574 which here encompasses experiments with higher-viscosity liquids (lowest *Re*) as well as experiments with low-
575 viscosity liquid and a high gas flux (highest *Re*), the drift velocity is low; the bubble and liquid move at a
576 similar velocity. In this case, the *K* value transitions to be an order of magnitude lower than for bubbly flow, and
577 we use this value to estimate Stromboli's drift velocity. Broadly speaking, the *K* value seems to indicate the gas
578 flow pattern and *K* values of ~1 are likely adequate for bubbly flow, regardless of the liquid's viscosity. In Fig.
579 8, this can be seen at either end of the plot, which correspond to experiments that developed a component of
580 slug flow, either due to the liquid viscosity (on the left end) or high gas flux (on the right end). The 1.53 value
581 defined by Harmathy is therefore used to approximate the drift velocity of bubbles in all of the other passively
582 degassing systems.
583
584 Combining equations 20 and 21, the estimated gas fractions for the selected volcanoes are approximately 0.19 -
585 0.44, for conduits that are on the order of meters in diameter (Table 2). As discussed in section 4.1, the model in
586 this study has some sensitivity to conduit diameter. This is also true for estimations of gas fraction, in which the
587 superficial gas velocity is strongly inversely proportional to conduit diameter. In this way, a volume of gas
588 passing through a fairly restricted aperture results in a greater concentration of gas compared to a wider aperture.

589 If the diameters are instead on the order of 10's of meters, the estimations of gas fraction made via this method
590 are generally lower, and range from 0.03 – 0.43.

Table 1 Explanation of symbols

Symbol	Description	Units
μ	viscosity	Pa·s
ρ	density	kg/m^3
$\Delta\rho$	density difference	kg/m^3
$\dot{m}$	mass flux	kg/s
Q	volumetric flux	m^3/s
v	velocity	m/s
D	diameter	m
L	length scale	m
h	depth (in conduit)	m
A	cross sectional area	m^2
ε	gas volume fraction	
P	pressure	MPa
M	molar mass	kg/mol
T	temperature	K
R	ideal gas constant	J/mol·K
g	gravitational constant	m/s^2
C	proportionality constant	
C_0	flow profile parameter	
K	flow pattern parameter	
Re	Reynolds number	
N_f	Dimensionless inverse viscosity	
Π	Dimensionless parameter	
	placeholder variable	
F, f	Function	
Subscript		
l	liquid	
g	gas	
c	conduit	
b	bubble	
s	superficial (velocity)	
d	drift (velocity) of a bubble	
model	analogue model	
magma	natural magma	
atm	atmospheric (pressure)	
spec	specie of volatile	

Table 2 Analogue volcano properties

	ρ_l (kg/m^3)	μ_l (Pa·s)	D_c (m)	Q_l (m^3/s)	$\dot{m}_g$ (kg/s)	$C0^{r*}$ -	$K^{s,t*}$ -	ε^*
Villarrica[a,b]	2524-2630	31-277	6.6-11.6	0.5-1.9	46-50	2.29	1.53	0.30-0.38
Nyiragongo[c,g]	2700	60	5	1.1-4.0	206-348	2.29	1.53	0.43
Erta Ale[d,e]	2700	100	5	0.1-0.3	18-26	2.29	1.53	0.35-0.37
Pu'u O'o[f,g,h]	2678-2685	100-500	3.5	0.6-0.8	315-420	2.29	1.53	0.43
Masaya[i,j]	2574-2679	630	4-12	1.0-16.9	23-420	2.29	1.53	0.21-0.43
Erebus[g,k,l]	2400-2700	10000	7	0.01-0.4	8-24	2.29	1.53	0.19-0.30
Stromboli[m,n,o]	2700-2750	300-14000	2.5-2.9	0.2	44-52	2.29	0.10	0.44
Ambrym[p,q]	1550-2700	596-1445	25	20.0	1504-2060	2.29	1.53	0.38-0.42

[a] Palma *et al.* (2011); [b] Sawyer *et al.* (2011) ; [c] Sawyer *et al.* (2008a); [d] Bouche *et al.* (2010); [e] Sawyer *et al.* (2008b); [f] Mittelstaedt and Garcia (2007); [g] Harris *et al.* (1999); [h] Sutton *et al.* (2001); [i] Stix (2007); [j] Rymer *et al.* (1998) ; [k] Oppenheimer *et al.* (2009); [l] Sweeney *et al.* (2008); [m] Lautze and Houghton (2007); [n] Burton *et al.* (2007); [o] Allard (2010); [p] Allard et al. (2015); [q] Allard et al. (2016); [r] Viana *et al.* (2003); [s] Harmathy (1960); [t] This study; [*] estimated via a formulation outlined in Pioli *et al.* (2012), see Appendix A

Table 3 Scaling for experiments and passively degassing, basaltic volcanoes

	Re (gas)	Re (liquid)	N_f
Passive degassing volc.	$10^{-1} – 10^3$	$10^{-4} – 10^3$	$1 – 10^3$
Experiments (syrup/air)	$10^{-3} – 10^{-1}$	$10^{-4} – 10^{-2}$	$10^{-1} – 10$
Experiments (mixture/air)	10 – 40	25 – 45	~400
Experiments (water/air)	$10^3 – 10^4$	$10^3 – 10^4$	$6x10^4$

Table 4 Experimental data

ρ_l (kg/m^3)	μ_l (Pa·s)	Q_g (L/min)	ε	D_b (cm)	v_b (cm/s)	v_l (cm/s)	Q_l (m^3/s)	Re_l	Re_g	N_f
Glucose										
1430	2.33E+02	0.4	0.135	5.94	0.79	0.07	2.5E-06	3.0E-04	2.0E-03	3.6E-01
1421	1.08E+02	0.4	0.072	5.05	1.38	0.12	4.4E-06	1.1E-03	5.9E-03	7.6E-01
1421	8.03E+01	0.4	0.053	4.98	2.33	0.16	6.0E-06	2.0E-03	9.4E-03	1.0E+00
1421	8.43E+01	0.8	0.109	5.93	2.62	0.21	7.1E-06	2.3E-03	1.2E-02	9.8E-01
1421	8.02E+01	0.8	0.072	5.43	2.81	0.16	5.7E-06	1.9E-03	1.6E-02	1.0E+00
1421	8.41E+01	1.2	0.151	6.02	3.36	0.20	6.6E-06	2.2E-03	1.6E-02	9.8E-01
1421	8.00E+01	1.2	0.113	5.39	3.73	0.28	9.6E-06	3.3E-03	1.9E-02	1.0E+00
1413	7.23E+01	0.4	0.032	4.53	2.01	0.08	3.1E-06	1.1E-03	1.3E-02	1.1E+00
1413	5.60E+01	0.4	0.011	4.15	4.63	0.11	4.2E-06	2.0E-03	2.9E-02	1.5E+00
1413	5.88E+01	0.8	0.043	5.05	4.45	0.15	5.5E-06	2.5E-03	2.8E-02	1.4E+00
1413	5.59E+01	0.8	0.027	4.49	5.20	0.18	6.7E-06	3.1E-03	3.7E-02	1.5E+00
1413	5.85E+01	1.2	0.063	5.27	6.26	0.45	1.6E-05	7.3E-03	3.5E-02	1.4E+00
1413	5.56E+01	1.2	0.053	5.12	6.19	0.45	1.6E-05	7.8E-03	4.0E-02	1.5E+00
1408	6.44E+01	0.4	0.068	4.03	2.57	0.09	3.2E-06	1.3E-03	1.0E-02	1.3E+00
1404	5.74E+01	0.4	0.022	3.63	2.97	0.11	4.3E-06	1.9E-03	2.0E-02	1.4E+00
1404	4.83E+01	0.4	0.006	3.35	8.06	0.20	7.6E-06	4.0E-03	4.7E-02	1.7E+00
1404	4.62E+01	0.8	0.043	4.41	8.19	0.35	1.3E-05	7.2E-03	3.6E-02	1.8E+00
1404	4.80E+01	0.8	0.016	3.95	10.00	0.25	9.6E-06	5.2E-03	5.5E-02	1.7E+00
1404	4.60E+01	1.2	0.063	4.60	9.47	0.43	1.6E-05	9.0E-03	4.4E-02	1.8E+00
1404	4.76E+01	1.2	0.032	4.47	11.36	0.40	1.5E-05	8.0E-03	6.0E-02	1.7E+00
1395	4.29E+01	0.4	0.006	3.81	7.32	0.15	5.6E-06	3.3E-03	5.3E-02	1.9E+00
1395	4.34E+01	0.4	0.027	3.12	11.10	0.17	6.3E-06	3.7E-03	2.4E-02	1.9E+00
1395	2.04E+01	0.8	0.011	3.91	13.40	0.40	1.5E-05	1.9E-02	1.6E-01	4.0E+00
1395	4.30E+01	0.8	0.032	3.43	13.47	0.39	1.4E-05	8.7E-03	4.4E-02	1.9E+00
1395	2.02E+01	1.2	0.027	4.22	14.61	0.61	2.3E-05	2.9E-02	1.5E-01	4.0E+00
1395	4.28E+01	1.2	0.043	3.71	14.66	0.37	1.4E-05	8.2E-03	5.8E-02	1.9E+00
1387	1.97E+01	0.4	0.006	3.09	11.42	0.28	1.1E-05	1.4E-02	1.2E-01	4.1E+00
1387	2.35E+01	0.4	0.006	2.81	16.38	0.50	1.9E-05	2.1E-02	9.6E-02	3.4E+00
1387	1.92E+01	0.8	0.032	2.98	16.82	0.51	1.9E-05	2.6E-02	9.8E-02	4.2E+00
1387	1.89E+01	0.8	0.043	4.25	16.82	0.43	1.6E-05	2.2E-02	8.6E-02	4.3E+00
1387	2.33E+01	0.8	0.016	3.13	19.12	0.46	1.7E-05	1.9E-02	1.1E-01	3.5E+00
1387	1.87E+01	1.2	0.043	4.28	19.37	0.65	2.4E-05	3.3E-02	1.3E-01	4.3E+00
1387	2.27E+01	1.2	0.027	3.97	22.73	0.80	3.0E-05	3.4E-02	1.4E-01	3.5E+00
1300	1.81E-01	0.4	0.006	2.15	29.55	5.03	1.9E-04	2.5E+01	1.2E+01	4.2E+02
1300	1.81E-01	0.8	0.016	2.22	34.99	6.10	2.3E-04	3.0E+01	1.4E+01	4.2E+02
1300	1.81E-01	1.2	0.022	3.32	37.73	6.57	2.5E-04	3.3E+01	1.8E+01	4.2E+02
1300	1.81E-01	2.3	0.016	3.12	44.09	6.54	2.5E-04	3.3E+01	3.9E+01	4.2E+02
1300	1.81E-01	3.4	0.048	3.32	42.53	7.27	2.7E-04	3.6E+01	3.4E+01	4.2E+02
1300	1.80E-01	4.5	0.058	4.00	47.44	8.68	3.1E-04	4.3E+01	4.1E+01	4.2E+02
Water										
998	1.00E-03	0.4	0.016	1.06	31.67	7.69	2.9E-04	5.3E+03	9.5E+02	5.8E+04

998	1.00E-03	0.4	0.006	1.11	31.88	9.09	3.5E-04	6.3E+03	1.6E+03	5.8E+04
998	1.00E-03	0.4	0.006	1.34	25.97	10.00	3.8E-04	7.0E+03	1.6E+03	5.8E+04
998	1.00E-03	0.8	0.027	1.37	25.45	11.54	4.3E-04	8.0E+03	1.5E+03	5.8E+04
998	1.00E-03	0.8	0.022	1.27	30.63	12.50	4.7E-04	8.6E+03	1.6E+03	5.8E+04
998	1.00E-03	0.8	0.016	1.91	32.69	11.54	4.4E-04	8.0E+03	1.9E+03	5.8E+04
998	1.00E-03	1.2	0.027	1.66	30.76	16.67	6.2E-04	1.1E+04	2.2E+03	5.8E+04
998	1.00E-03	1.2	0.027	1.60	30.42	12.00	4.5E-04	8.3E+03	2.2E+03	5.8E+04
998	1.00E-03	1.2	0.016	2.28	29.86	14.29	5.4E-04	9.9E+03	2.8E+03	5.8E+04
998	1.00E-03	1.8	0.043	1.81	36.22	17.65	6.5E-04	1.2E+04	2.6E+03	5.8E+04
998	1.00E-03	1.8	0.032	2.13	32.66	15.79	5.9E-04	1.1E+04	3.0E+03	5.8E+04
998	1.00E-03	1.8	0.032	2.32	41.25	15.00	5.6E-04	1.0E+04	3.0E+03	5.8E+04
998	1.00E-03	2.4	0.048	2.22	36.29	20.00	7.3E-04	1.4E+04	3.3E+03	5.8E+04
998	1.00E-03	2.4	0.037	2.03	40.28	10.00	3.7E-04	6.9E+03	3.8E+03	5.8E+04
998	1.00E-03	2.4	0.032	2.41	37.36	15.00	5.6E-04	1.0E+04	4.0E+03	5.8E+04
998	1.00E-03	3.0	0.058	2.27	38.42	25.00	9.1E-04	1.7E+04	3.8E+03	5.8E+04
998	1.00E-03	3.0	0.043	2.46	35.41	23.08	8.5E-04	1.6E+04	4.4E+03	5.8E+04
998	1.00E-03	3.0	0.037	2.29	34.13	17.65	6.5E-04	1.2E+04	4.7E+03	5.8E+04
998	1.00E-03	3.5	0.063	2.08	43.46	17.65	6.4E-04	1.2E+04	4.2E+03	5.8E+04
998	1.00E-03	3.5	0.053	2.31	40.93	21.43	7.8E-04	1.5E+04	4.6E+03	5.8E+04
998	1.00E-03	3.5	0.053	2.39	42.53	18.75	6.8E-04	1.3E+04	4.6E+03	5.8E+04
998	1.00E-03	4.0	0.072	2.46	36.99	30.00	1.1E-03	2.0E+04	4.5E+03	5.8E+04
998	1.00E-03	4.0	0.063	1.98	40.00	20.00	7.2E-04	1.4E+04	4.8E+03	5.8E+04
998	1.00E-03	4.0	0.067	2.45	45.00	21.43	7.7E-04	1.4E+04	4.7E+03	5.8E+04
998	1.00E-03	4.5	0.086	2.35	39.39	30.00	1.1E-03	2.0E+04	4.6E+03	5.8E+04
998	1.00E-03	4.5	0.063	2.37	37.55	20.00	7.2E-04	1.4E+04	5.4E+03	5.8E+04
998	1.00E-03	4.5	0.067	2.70	35.69	30.00	1.1E-03	2.0E+04	5.2E+03	5.8E+04

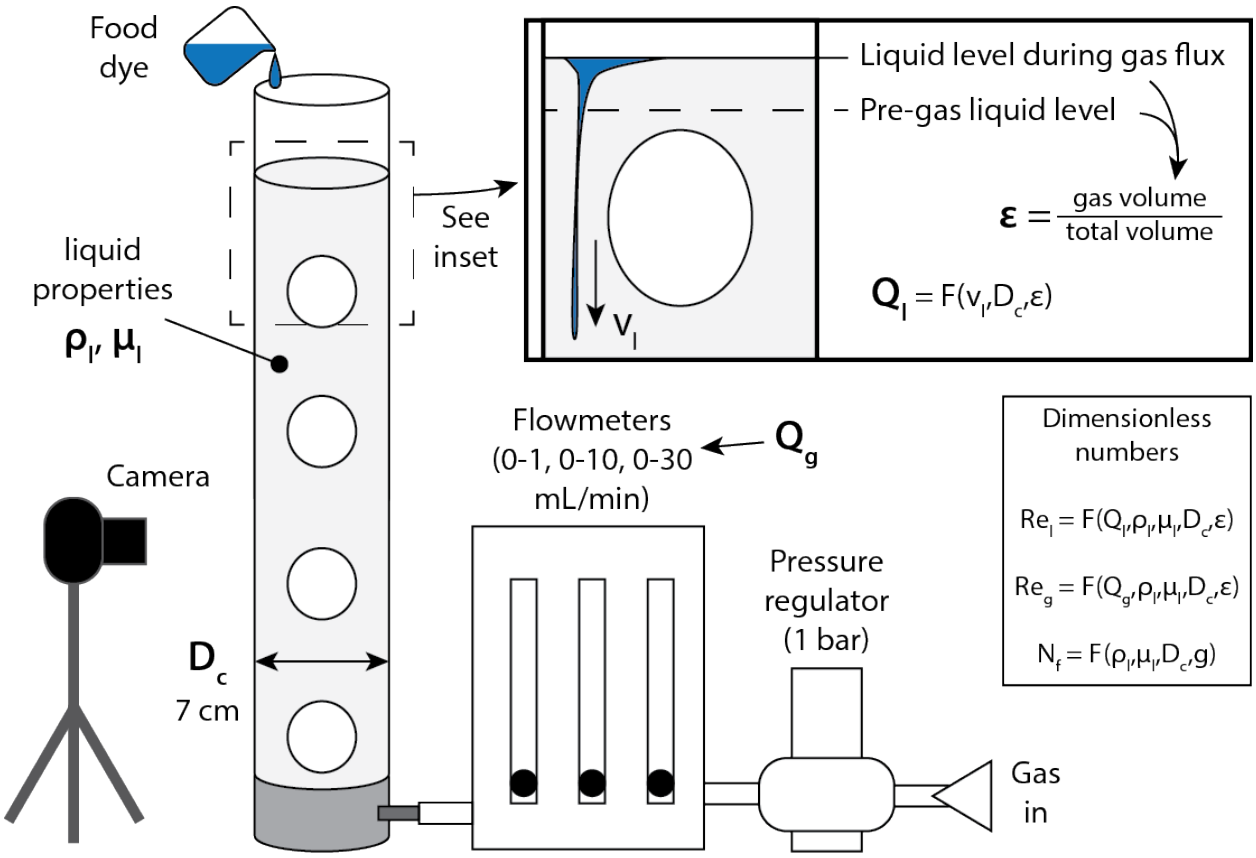
Food dye
liquid properties
ρ_l, μ_l
See inset
Liquid level during gas flux
Pre-gas liquid level
$\varepsilon = \frac{\text{gas volume}}{\text{total volume}}$
$Q_l = F(v_l, D_c, \varepsilon)$
v_l
Flowmeters (0-1, 0-10, 0-30 mL/min)
Q_g
Camera
D_c 7 cm
Pressure regulator (1 bar)
Gas in
Dimensionless numbers
$Re_l = F(Q_l, \rho_l, \mu_l, D_c, \varepsilon)$
$Re_g = F(Q_g, \rho_l, \mu_l, D_c, \varepsilon)$
$N_f = F(\rho_l, \mu_l, D_c, g)$

Fig. 1

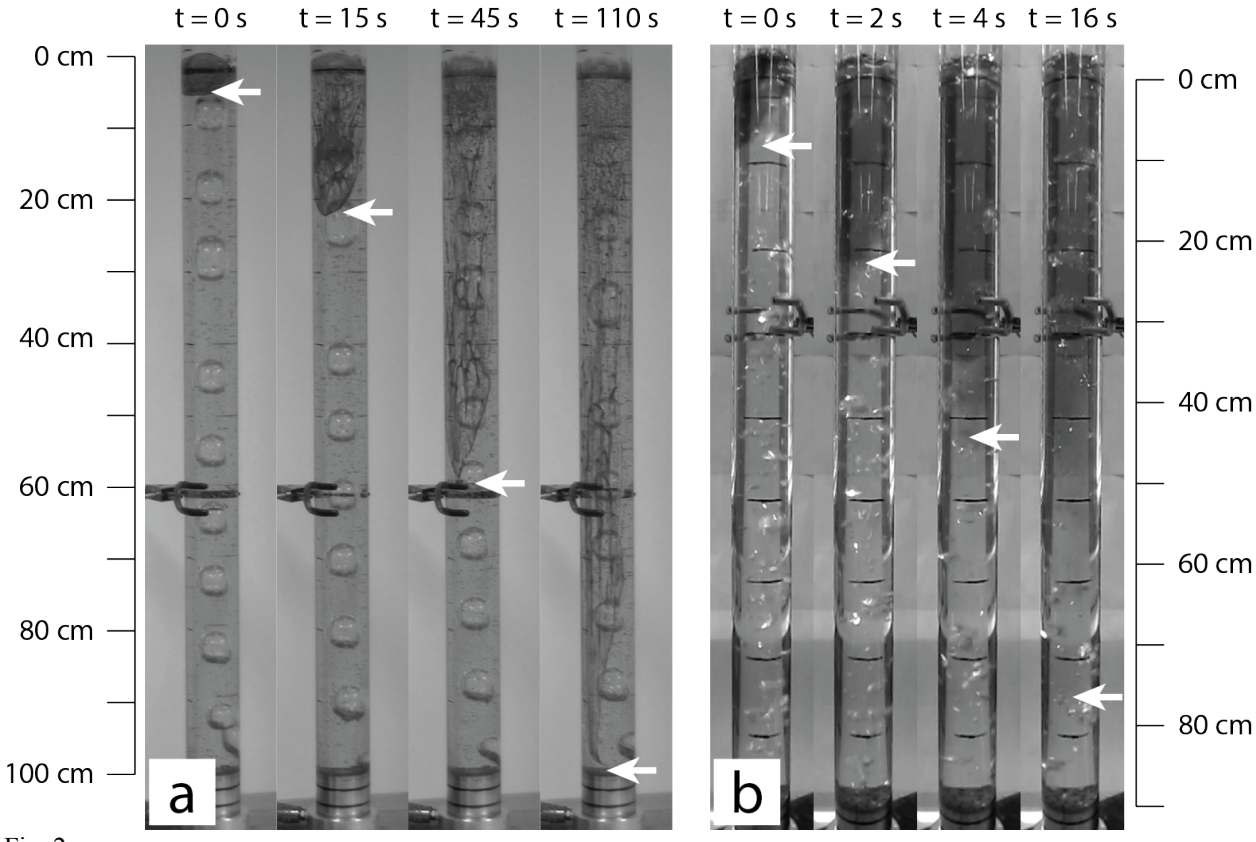
t = 0 s
t = 15 s
t = 45 s
t = 110 s
t = 0 s
t = 2 s
t = 4 s
t = 16 s
0 cm
20 cm
40 cm
60 cm
80 cm
100 cm
a
b

Fig. 2

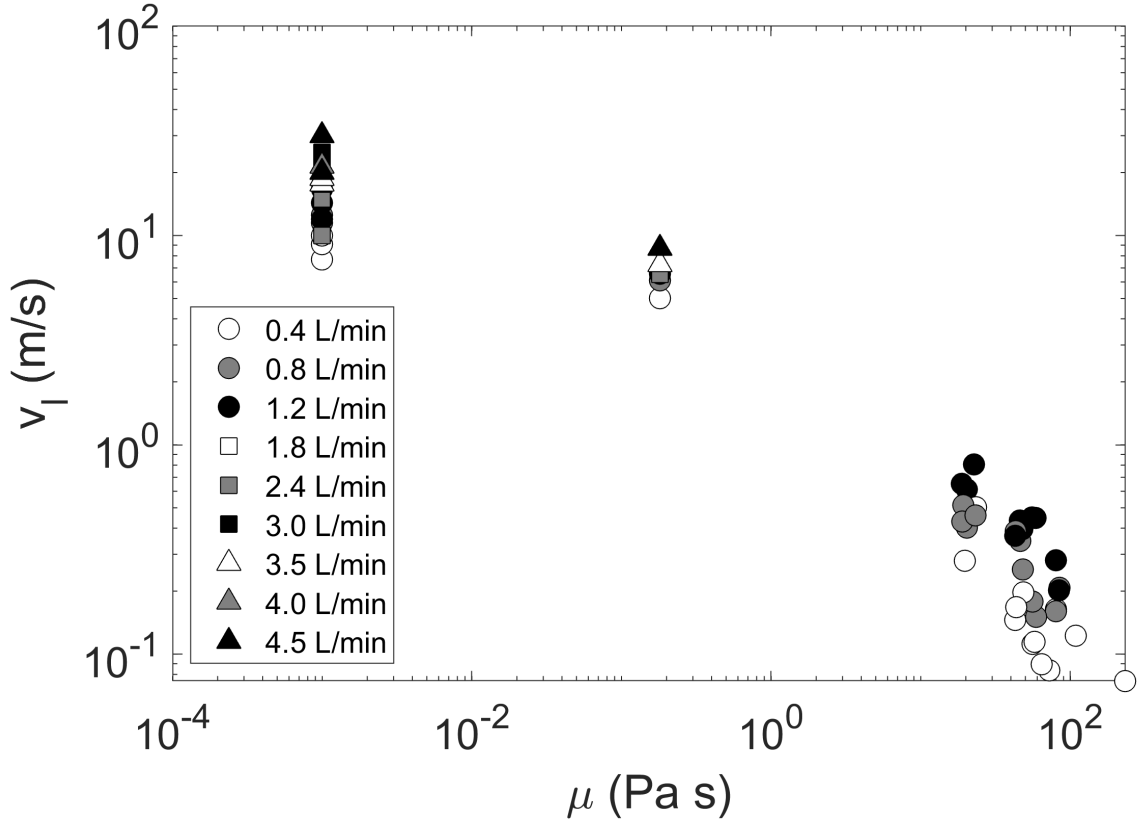
10^2
10^1
10^0
10^{-1}
v_l (m/s)
0.4 L/min
0.8 L/min
1.2 L/min
1.8 L/min
2.4 L/min
3.0 L/min
3.5 L/min
4.0 L/min
4.5 L/min
10^{-4}
10^{-2}
10^0
10^2
μ (Pa s)

Fig. 3

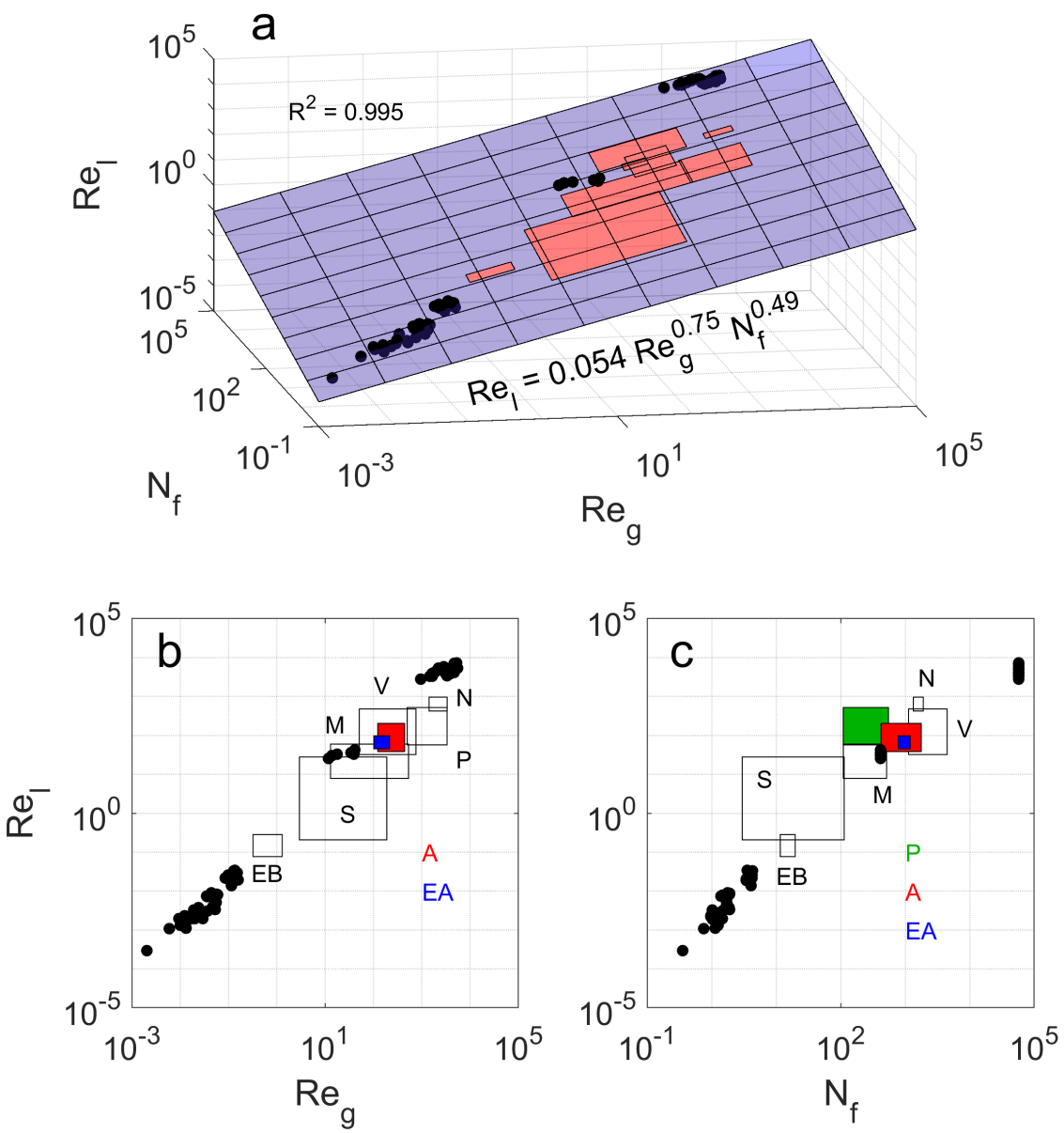

Fig. 4

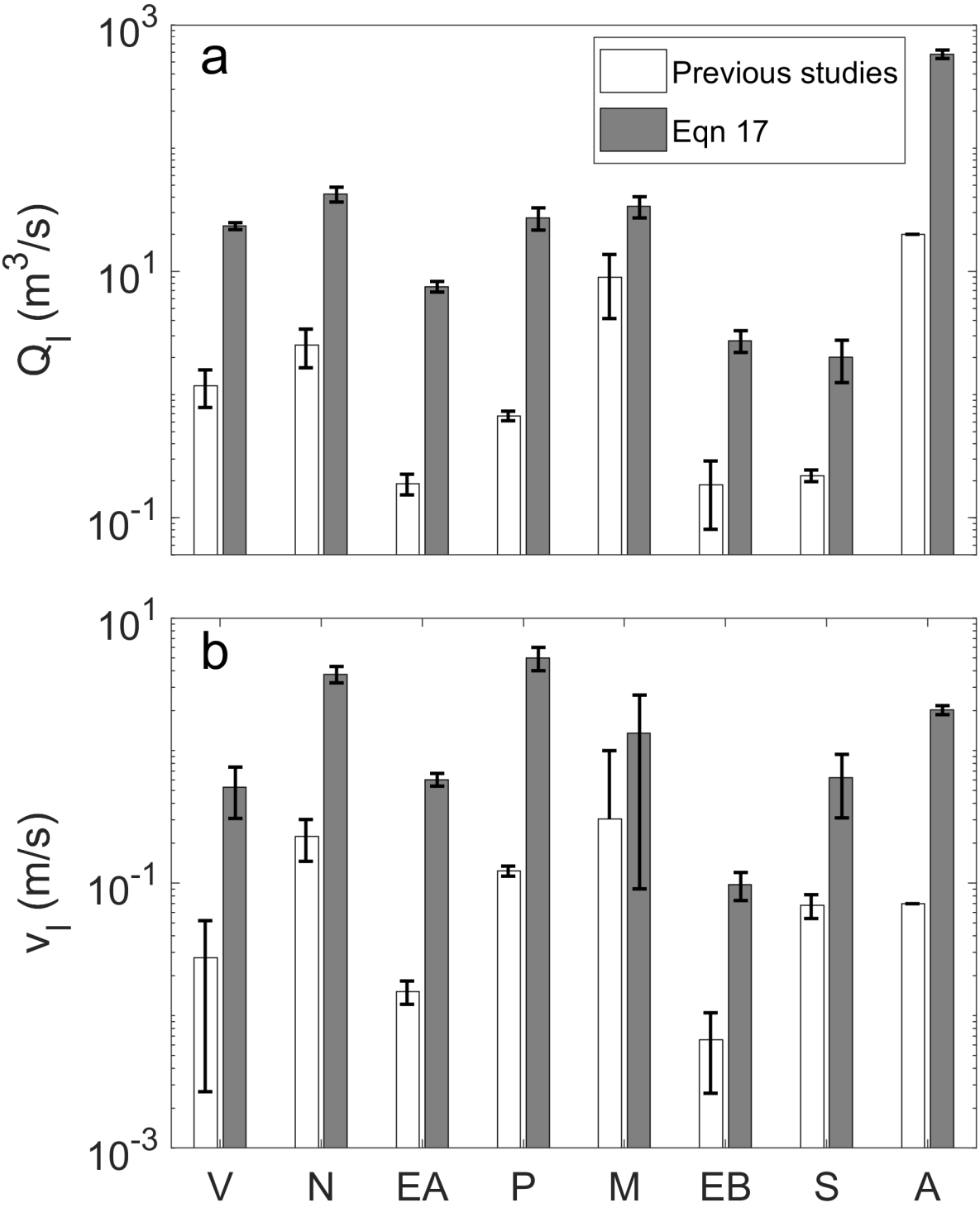
a
Previous studies
Eqn 17
10^3
10^1
10^{-1}
Q_l (m^3/s)
b
10^1
10^{-1}
10^{-3}
v_l (m/s)
V
N
EA
P
M
EB
S
A

Fig. 5

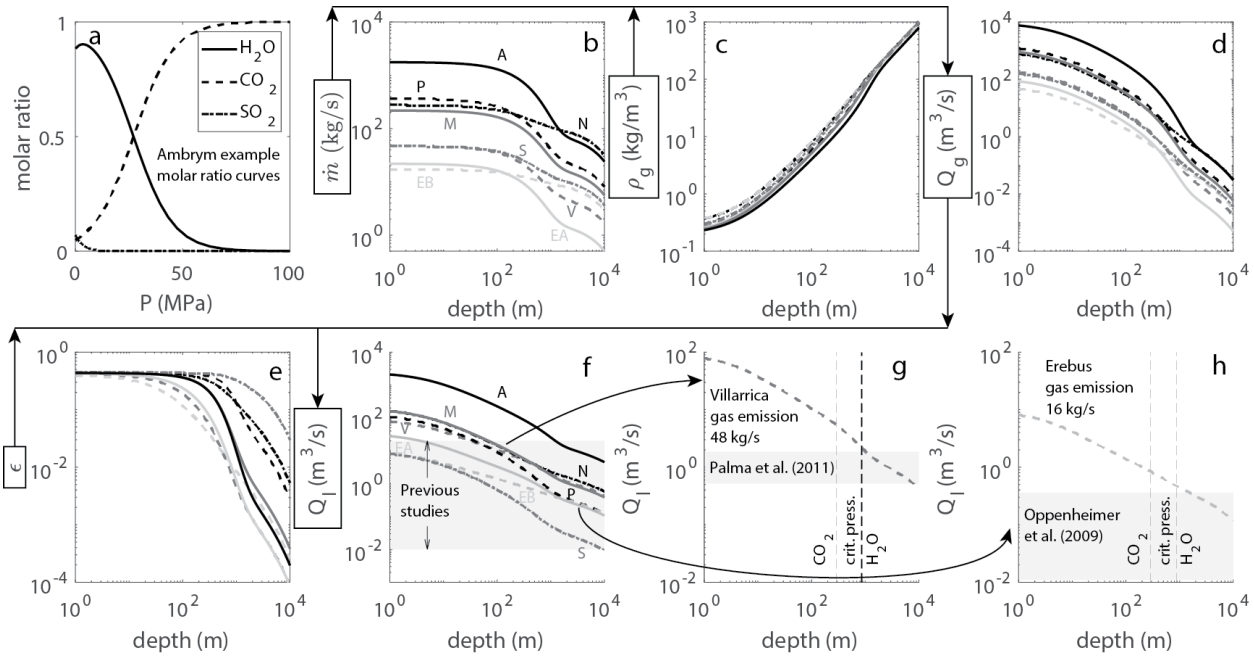
a
molar ratio
P (MPa)
H2O
CO2
SO2
Ambrym example
molar ratio curves
b
ṁ (kg/s)
depth (m)
A
P
M
N
S
EB
V
EA
c
ρg (kg/m3)
depth (m)
d
Qg (m3/s)
depth (m)
e
ϵ
QI (m3/s)
depth (m)
f
QI (m3/s)
depth (m)
Previous
studies
g
QI (m3/s)
depth (m)
Villarrica
gas emission
48 kg/s
Palma et al. (2011)
CO2
crit. press.
H2O
h
QI (m3/s)
depth (m)
Erebus
gas emission
16 kg/s
Oppenheimer
et al. (2009)
CO2
crit. press.
H2O

Fig. 6

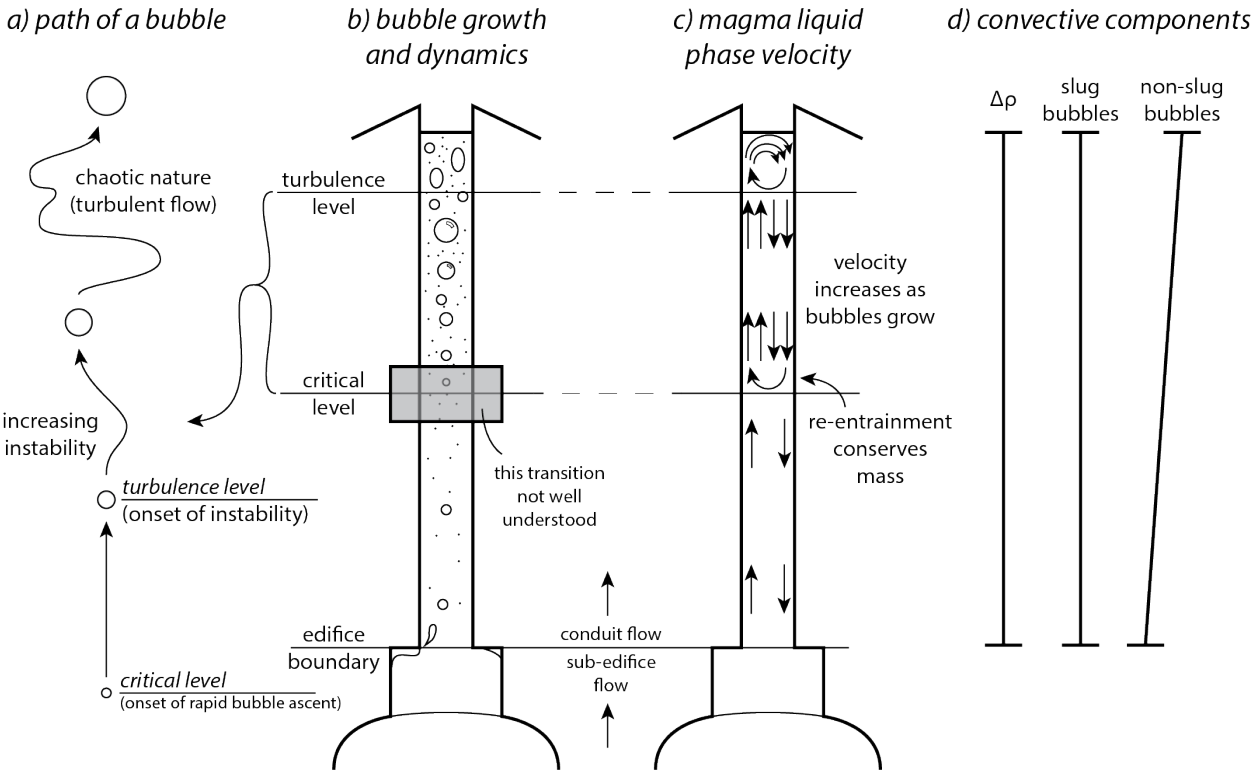
a) path of a bubble
b) bubble growth
and dynamics
c) magma liquid
phase velocity
d) convective components
chaotic nature
(turbulent flow)
turbulence
level
critical
level
increasing
instability
turbulence level
(onset of instability)
critical level
(onset of rapid bubble ascent)
this transition
not well
understood
velocity
increases as
bubbles grow
re-entrainment
conserves
mass
edifice
boundary
conduit flow
sub-edifice
flow
Δρ
slug
bubbles
non-slug
bubbles

Fig. 7

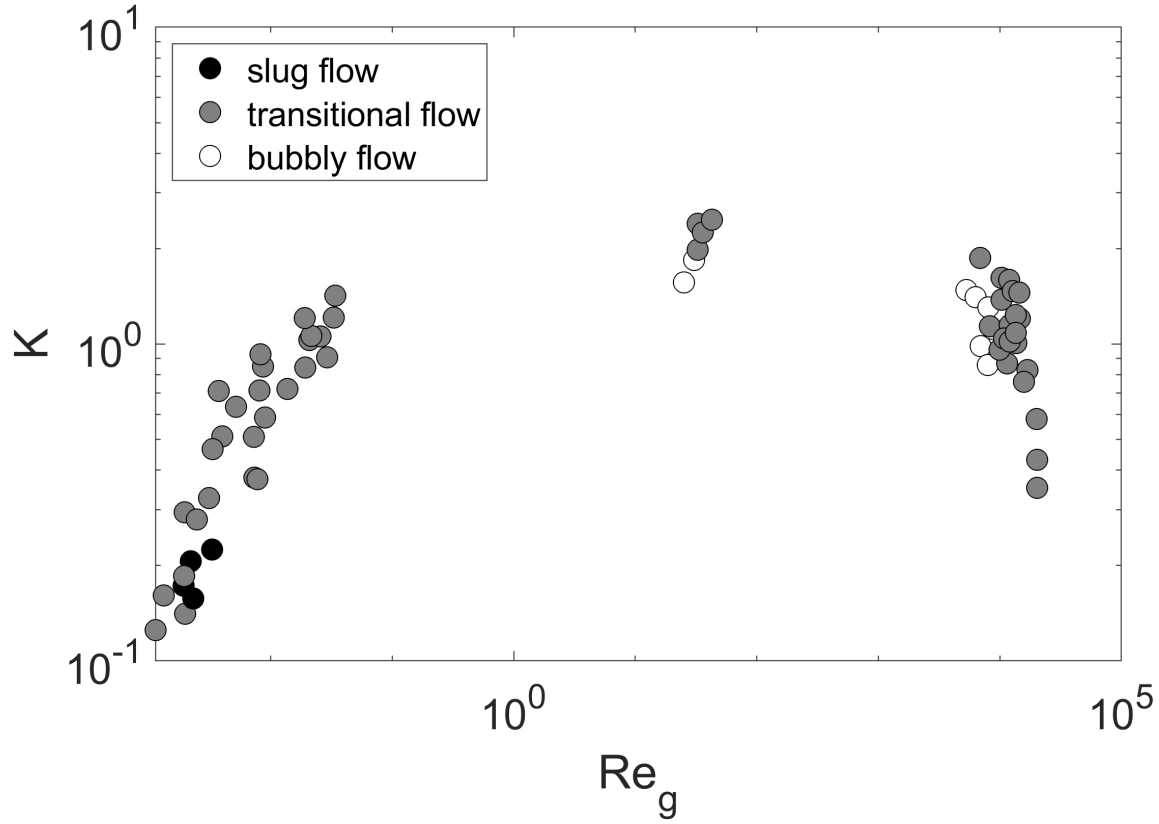
slug flow
transitional flow
bubbly flow
K
Re_g
10^1
10^0
10^-1
10^0
10^5

Fig. 8